Aerosol Vertical Mass Flux Measurements During Heavy Aerosol Pollution Episodes at a Rural Site and an Urban Site in the Beijing Area of the North China Plain

Renmin Yuan[1], Xiaoye Zhang[2, 4], Hao Liu[1], Yu Gui[1], Bohao Shao[1], Xaioping Tao[5], Yaqiang Wang[2], Junting Zhong[2], Yubin Li[3] and Zhiqiu Gao[3]

[1]School of Earth and Space Sciences, University of Science and Technology of China, Anhui, 230026, China

[2]State Key Laboratory of Severe Weather & Key Laboratory of Atmospheric Chemistry of CMA, Chinese Academy of Meteorological Sciences, Beijing 100081, China

[3]School of Geography and Remote Sensing, Nanjing University of Information Science and Technology, Nanjing 210044, China

[4]Center for Excellence in Regional Atmospheric Environment, IUE, CAS, Xiamen 361021, China.

[5]School of Physical Sciences, University of Science and Technology of China, Anhui, 230026, China

Correspondence: Renmin Yuan (rmyuan@ustc.edu.cn) and Xiaoye Zhang (xiaoye@cma.gov.cn)

Abstract:

Due to excessive anthropogenic emissions, heavy aerosol pollution episodes (HPEs) often occur during winter in the Beijing-Tianjin-Hebei (BTH) area of the North China Plain. Extensive observational studies have been carried out to understand the causes of HPEs; however, few measurements of aerosol vertical fluxes exist, despite them being the key to understanding vertical aerosol mixing, specifically during weak turbulence stages in HPEs. In the winter of 2016 and the spring of 2017, based on the light propagation theory and surface-layer similarity theory, aerosol vertical mass fluxes were measured by combining large aperture scintillometer (LAS) observations, surface $PM_{2.5}$ and PM_{10} mass concentrations, and meteorological observations, including temperature, relative humidity (RH), and visibility, at a rural site in Gucheng (GC), Hebei Province, and an urban site at the Chinese Academy of Meteorological Sciences (CAMS) in Beijing located 100 km to the northeast. The near-ground aerosol mass flux was generally lower in winter than in spring and weaker in rural GC than in urban Beijing. This finding provides direct observational evidence from the perspective of vertical aerosol fluxes for a weakened turbulence intensity in winter and in polluted areas such as GC. The HPEs included a transport stage (TS), an accumulative stage (AS), and a removal stage (RS). During the HPEs from January 25, 2017 to January 31, 2017, in Beijing, the mean mass flux decreased by 51% from 0.0049 mg m^{-2}s^{-1} in RSs to 0.0024 mg m^{-2}s^{-1} in the TSs. During the ASs, the mean mass flux decreased further to 0.00087 mg m^{-2}s^{-1}, accounting for approximately 1/3 of the flux in the TSs. A similar reduction from the TSs to ASs was observed in the HPE from December 16, 2016 to December 22, 2016 in GC. The weakened mass flux indicates that the already weak turbulence would be further weakened by aerosol pollution to a certain extent, which would further facilitate aerosol accumulation.

1 Introduction

Recently, due to the country's rapid development of industrialization and urbanization, China has experienced heavy aerosol pollution episodes (HPEs), particularly in the Beijing, Tianjin and Hebei (BTH) region, which is one of the most polluted areas in China (Zhang et al., 2012). The HPEs often last for a long duration in the BTH region and cover a wide area, particularly in winter; they also severely reduce near-ground visibility (Lei and Wuebbles, 2013) and can have detrimental effects on public health (He et al., 2018;Cao et al., 2012). This heavy pollution weather has received extensive attention in recent years, and many observational studies have been carried out (Zhong et al., 2018a;Sun et al., 2014;Wang et al., 2015;Guo et al., 2011;Zhang et al., 2009b;Huang et al., 2014). Modelling studies have also been performed to examine the regional transport of pollutants (Wang et al., 2014) and to study the important role of large-eddy convective turbulent mixing in the vertical transfer of pollutants from a field campaign in Beijing (Li et al., 2018). However, few studies on the turbulence contribution of the aerosol transport flux in the surface layer have been conducted.

Ground pollutant emissions are known as the main source of aerosols in the atmosphere. However, in previous studies, no measurements of ground emissions during heavy pollution events were collected. Surface emission data are currently required for model verification and pollution predictions, and these data are primarily obtained through emission inventories (Wu et al., 2012;Bond et al., 2004). The establishment of emission inventories is primarily based on emission activity and emission factor (EF) data (Akagi et al., 2011;Lu et al., 2011;Roden et al., 2006;Zhang and Tao, 2009). Emissions data are mainly obtained from statistical yearbooks (Zhang et al., 2009a). Some studies have used fixed EFs while others have implemented dynamic EFs (Bond et al., 2004;Zhang et al., 2009a). Many factors are considered in dynamic EFs, such as the size of a city, the degree of economic development, the type of fuel, the type of technology, the consumption of a product, the control technology, and so on, as well as estimates based on actual measured meteorological parameters and aerosol parameters (Chen et al., 2015;Karvosenoja et al., 2008;Shen et al., 2013). A numerical model has also been used to estimate average fleet emission factors in typical urban conditions (Ketzel et al., 2003;Krecl et al., 2018). The error in aerosol fluxes based on the use of emission inventories is very large (Liu et al., 2017;Zheng et al., 2017). Emission inventories constructed using the EF method provide only the total emission amount of atmospheric pollutants within a region. However, the emission data should be gridded to a suitable scale for air quality modelling and pollution predictions. Thus, near-surface aerosol emission data with a higher temporal and spatial resolution are urgently needed.

Many methods have been used to obtain aerosol flux data. For the upward transport of aerosols near the surface layer, the aerodynamic method was adopted in the early years, and the aerosol concentration gradient at different heights was measured and then calculated based on the similarity theory of the near-surface layer or calculated by the boundary layer box model, which can be based on meteorological data (Ceburnis et al., 2016;Hourdin et al., 2015;Zhang and Li, 2014). The emission rates of bioaerosols were also estimated from spore counts and molecular tracers (Elbert et al., 2007). The abundance of microbes and meteorological data were measured, and an estimate may be derived of the sea-air exchange of microorganisms (Mayol et al., 2014).

With the use of instruments for measuring the number of aerosol particles during recent years (for example, the GP-WCPC3787 particle counter by TSI), the eddy covariance (EC) method has been applied, and measurements of the aerosol particle number flux have become possible. The

80   vertical transport flux of the aerosol particle number density F_p is denoted as a cross-correlation
81   between the aerosol particle number concentration N' and the vertical wind speed w' (Ripamonti et
82   al., 2013). Based on this principle, the vertical velocity fluctuations and the fluctuations in the
83   aerosol particle number density can be measured. As a result, the vertical transport flux of the
84   aerosol particle number density has been measured in many cities, such as in Toronto, Canada
85   (Gordon et al., 2011), Stockholm, Sweden (Vogt et al., 2011b), Helsinki, Finland (Ripamonti et al.,
86   2013), London, UK (Harrison et al., 2012), the Blodgett Forest Observatory in the United States
87   (Farmer et al., 2011), and measurements of sea salt aerosol fluxes in northern Europe (Brooks et al.,
88   2009;Sproson et al., 2013). These results have shown the quantitative relationship among urban
89   aerosol fluxes, urban vehicle emissions, and meteorological conditions (Jarvi et al., 2009) and have
90   been used to determine sea salt aerosol transport characteristics and provide further knowledge of
91   aerosol properties (Nemitz et al., 2009).These measurements have been mainly collected in cities
92   because of their anthropogenic contributions to aerosol emissions. These data can be used as routine
93   model inputs. Direct eddy covariance measurements of aerosol exchanges in tropical forests, where
94   primary biological aerosol particles represent a substantial fraction of the airborne particulate matter
95   (Graham et al., 2003), were also performed by Ahlm et al. (2010a and 2010b) and Whitehead et al.
96   (2010), potentially giving a proxy for microbial emissions in tropical ecosystems.

97   Although measurements of urban aerosol particle number density fluxes have been collected,
98   the current eddy correlation method only provides fluxes for the aerosol particle number density at
99   a point. We know that the underlying surface of a city is very complex, and thus the aerosol particle
100 flux is not homogeneous in the horizontal. For a complex underlying surface such as a city, these
101 point measurements are not very representative. Therefore, it is of great importance to design an
102 aerosol flux measurement system with an accurate spatial representation.

103   The use of eddy correlation principles to measure sensible heat fluxes has been widely
104 performed (Lee, 2004). Current sensible heat fluxes can also be obtained using a large aperture
105 scintillometer (LAS) based on the light propagation theory and similarity theory (Zeweldi et al.,
106 2010). This configuration makes it is possible to achieve aerosol mass flux measurements using the
107 light propagation theory and similarity theory. Recently, we measured the imaginary part of the
108 atmospheric equivalent refractive index structure parameter based on the light propagation theory
109 (Yuan et al., 2015). The results showed that the imaginary part of the atmospheric equivalent
110 refractive index structure parameter is related to turbulent transport and the spatial distribution
111 characteristics of aerosols. Experiments also showed that there is a strong correlation between the
112 imaginary part of the atmospheric equivalent refractive index and the mass concentration of aerosol
113 particles (Yuan et al., 2016). Thus, similar to the temperature structure parameter reflecting the
114 sensible heat flux, the structural parameter of the imaginary part of the atmospheric equivalent
115 refractive index can reflect the mass flux of aerosol particles. This paper attempts to measure the
116 aerosol mass flux in the BTH area.

117   To gain a deeper understanding of the interaction between atmospheric heavy pollution and
118 weather in the BTH region, joint observations have been carried out in the BTH region since the
119 winter of 2016 (Zhong et al., 2018b;Zhong et al., 2018a;Wang et al., 2018;Shen et al., 2018). The
120 observations reveal the large-scale and mesoscale transport processes of aerosols between heavy
121 pollution episodes (HPEs) in the BTH region in the winter of 2016. Most HPEs in the BTH region
122 are due to horizontal transport and unfavourable meteorological conditions (Zhong et al., 2018a).
123 However, during HPEs, no research has been conducted in the BTH area on quantifying the

124 contribution of surface emissions to the concentration of pollutants. In this study, we focus on HPEs

125 through field observations of aerosol transport based on the light propagation theory and surface

126 similarity in the Beijing urban district and Gucheng suburban area.

127 The second section of this paper introduces the theory of aerosol vertical transport flux

128 measurements, the third section introduces the experiment, the fourth section gives the experimental

129 results, and finally, the conclusion and discussion are presented in the fifth section.

130 ## 2 Theory and methods

131 The theory for calculating the vertical flux of aerosol particles and the theory for calculating

132 the friction velocity and characteristic temperature using the temperature and wind profiles is

133 presented in the following subsections.

134 ### 2.1 Calculation of the aerosol mass vertical flux

135 According to the micrometeorological principle (Stull, 1988), similar to the estimation method

136 of the sensible heat flux, the aerosol flux F_a can be obtained as follows:

137
$$F_a = u_* M_* \tag{1}$$

138 where u_* is the friction velocity, which can be obtained from the temperature and wind speed

139 profiles or directly from three-dimensional wind speed measurements; see Sec. 2.2. Prior

140 experiments have shown that the motion characteristics of aerosol particles in the atmosphere

141 approximate the motion of general scalars (Martensson et al. 2006; Vogt et al. 2011b). Therefore,

142 aerosol particles can be approximated as scalars, and characteristic parameters M_* similar to the

143 scalars can be introduced, which can be regarded as the atmospheric aerosol mass concentration

144 scale in the surface layer and deduced from surface layer similarity theory. This approximation is

145 similar to the surface-layer temperature scale (Stull, 1988) as follows:

146
$$\frac{C_M^2 (z-d)^{2/3}}{M_*^2} = \eta(\xi) \tag{2}$$

147 where z is the measurement height, d is the zero-displacement height (Evans and De Bruin,

148 2011;Hartogensis et al., 2003), $\xi=(z-d)/L$ is the nondimensional stability parameter, L is the Monin-

149 Obukhov (M-O) length and defined as $L = \frac{\bar{T} u_*^2}{\kappa g T_*}$ (Stull, 1988), $\bar{T}$ is the average temperature, T_*

150 is the surface-layer characteristic temperature, κ is the von Karman constant, which is 0.4, and g is

151 acceleration due to gravity. The stability function ($\eta(\xi)$) can be expressed as follows depending

152   on the stability condition (DeBruin et al., 1995):

$$\eta(\xi) = a_1[1 - a_2\xi]^{-2/3} \qquad (3)$$

154   for unstable conditions ($\xi < 0$), and the following:

$$\eta(\xi) = b_1[1 + b_2(\xi)^{e_1}] \qquad (4)$$

156   for stable conditions ($\xi >= 0$) (Wyngaard et al., 1971).

157   In Eqs. (3) and (4), a_1, a_2, b_1, b_2 and e_1 are constants, and different experiments have provided

158   different values, although the differences between these results are small. Here, we take the

159   parameters $a_1 = 4.9$, $a_2 = 9$, $b_1 = 5$, and $b_2 = 0$ (DeBruin et al., 1995).

160   C_M^2 in Eq. (2) is the aerosol mass concentration structure parameter. We assume that the

161   aerosol particles in the atmosphere follow the movement of the air and satisfy the turbulent motion

162   law. Previous studies have shown that the particle concentration fluctuation spectra follow a '-5/3'

163   power law under unstable stratification conditions (Martensson et al., 2006; Vogt et al., 2011b), and

164   the velocity-concentration co-spectra follows a '-4/3' power law (Martensson et al., 2006;Vogt et

165   al., 2011a;Kaimal et al., 1972). Thus, the distribution of small particles can be considered as a

166   conservative passive quantity analogous to the temperature. Then, at a separation (r) of the order in

167   the inertial subrange in a locally isotropic field, the aerosol mass concentration (denoted as M_a)

168   structure function ($D_M(r)$) follows a "2/3 law" (Wyngaard, 2010) and can be expressed as

169    $D_M(r) = \overline{[M_a(x) - M_a(x+r)]^2} = C_M^2 r^{2/3}$, where x is the position vector, r is the separation vector,

170   and the overbar indicates the spatial average.

171   The following describes the method to deduce the aerosol mass concentration structure

172   parameter C_M^2.

173   We assume that the aerosol particles are continuously dispersed in the air. The aerosol particles

174   and gases in the atmosphere can be considered as an equivalent medium, and an atmospheric

175   equivalent refractive index (AERI) n_{equ} is introduced that contains the real part n_{re} and the imaginary

176   part n_{im} of the equivalent refractive index. Thus, $n_{equ} = n_{re} + i \cdot n_{im}$. For visible light, the attenuation of

177   light by gases in the atmosphere is very weak; the cause of the attenuation is the absorption and

178   scattering due to aerosol particles. Therefore, the real part of the equivalent medium of aerosol

179   particles and gases is determined by the gas composition of the air. The fluctuation of the real part

180   is mainly determined by temperature fluctuations; the imaginary part is determined by the aerosol

181 particles, and the fluctuation of the imaginary part is determined by fluctuations in the aerosol

182 concentration.

183   For visible light, there is a strong linear relationship between the variation of the real part of

184 the AERI and the variation of the atmospheric temperature, i.e., $R_{_{TN}} = \dfrac{\delta T}{\delta n_{\mathrm{Re}}}$; thus, we have the

185 following:

186
$$R_{_{TN}} = -1.29 \times 10^{4} \times (1 + \frac{7.52 \times 10^{-3}}{\lambda^{2}})^{-1} \frac{\overline{T}^{2}}{\overline{P}} \qquad (5)$$

187 which is based on the relationship between the real part of the AERI (n_{Re}) and atmospheric
188 temperature (Tatarskii, 1961). Because the wavelength is deterministic, the ratio R_{TN} can be obtained
189 by measuring the atmospheric temperature. The imaginary part of the AERI has a close
190 correspondence with the extinction coefficient of the equivalent medium, and the extinction
191 coefficient is inversely proportional to the visibility. Higher concentrations of aerosols in the
192 atmosphere are related to lower visibility and vice versa; thus, the relationship between the
193 imaginary part of the AERI and the atmospheric aerosol mass concentration can be established. The
194 ratio of the atmospheric aerosol mass concentration to the imaginary part of the AERI R_{MN} can be
195 defined as follows:

196
$$R_{_{MN}} = \frac{M_{a}}{n_{_{Im}}} . \qquad (6)$$

197   Theoretical analysis has revealed that R_{MN} is associated with the aerosol particle size

198 distribution, mass density of the aerosol particles, and the aerosol particle refractive index. Because

199 of the relatively small variations in particle size and aerosol refractive index (Dubovik et al., 2002),

200 R_{MN} can be treated as a constant for surface-layer aerosols at a given location. M_a approximates the

201 PM$_{10}$ value. The variable n_{im} can be calculated as follows (Yuan et al., 2016):

202
$$n_{_{Im}} = \frac{0.55e - 6}{4\pi} \cdot \frac{3.912}{L_{V}} \qquad (7)$$

203 where the unit of visibility (L_V) is m.

204   According to Eqs. (5) and (6), we have the following:

205
$$C_{T}^{2} = R_{TN}^{2} C_{n.\mathrm{Re}}^{2} \qquad (8)$$

206
$$C_{M}^{2} = R_{MN}^{2} C_{n,\mathrm{Im}}^{2} \qquad (9)$$

207   Thus, the temperature structure parameter C_T^2 and the aerosol mass concentration fluctuation

208 structure parameter C_M^2 are converted into the measurement of the real and imaginary structurel

209   parameters of the AERI.

210   The measurement of relevant parameters is performed based on the light propagation theory.

211   When light is transmitted in an equivalent medium, the AERI fluctuation will cause fluctuations in

212   light intensity. Theoretical and experimental results have shown that the intensity fluctuation can be

213   decomposed into high-frequency and low-frequency fluctuations. The high-frequency fluctuations

214   are determined by fluctuations of the real part of the AERI, and the low-frequency fluctuations are

215   determined by fluctuations of the imaginary part of the AERI. Thus, the real and imaginary structure

216   parameters of the equivalent refractive index can be calculated by our developed LAS.

217   So far, we have completed the estimation of the aerosol mass transport flux.

218   According to the previous derivation and analysis, there are two calculation schemes for

219   determining the aerosol mass flux as follows:

220
$$F_{a1} = (\frac{C_{n,\mathrm{Im}}^2}{C_{n.\mathrm{Re}}^2})^{1/2} \frac{R_{MN}}{R_{TN}} u_* |T_*| \tag{10}$$

221
$$F_{a2} = u_* \sqrt{\frac{C_M^2 z^{2/3}}{\eta(\xi)}} = u_* R_{MN} \sqrt{\frac{C_{n,\mathrm{Im}}^2 z^{2/3}}{\eta(\xi)}} \tag{11}$$

222   When the free convection approximation $(-\xi \gg 1)$ is assumed, based on the definition of the

223   M-O length, and the similarity theory (Wyngaard et al., 1971), the following can be obtained:

224
$$F_{a3} = a(\frac{g}{\overline{T}})^{1/2} R_{TN}^{1/2} (C_{n,\mathrm{Re}}^2)^{1/4} R_{MN} (C_{n,\mathrm{Im}}^2)^{1/2} (z-d) \tag{12}$$

225   where the coefficient $a = a_1^{-3/4} a_2^{1/2} \kappa^{1/2}$ can be taken as 0.567 (DeBruin et al., 1995;Lagouarde et

226   al., 2006). Eqs. (10)-(12) are the theoretical basis for the aerosol mass flux measurements.

227   According to Eqs. (10)-(12), the vertical transport flux of aerosol particles is related to the

228   strength of turbulent fluctuations and aerosol mass concentration fluctuations.

229   **2.2 Calculation of the friction velocity and surface-layer characteristic temperature**

230   To calculate the aerosol vertical transport flux, according to Eq. (10), the values of the friction

231   velocity u_* and the characteristic temperature T_* are required. These can be obtained via wind speed

232   and temperature profile data. From the near-surface similarity theory, the temperature and wind

233   speed data measured at two heights of z_1 and z_2 can be used in the expressions of the friction velocity

234   u_* and the characteristic temperature T_* (Stull, 1988) as follows:

235
$$u_* = \frac{\kappa[U(z_2) - U(z_1)]}{\ln\frac{z_2}{z_1} - \Psi_U(\xi_2) + \Psi_U(\xi_1)} \tag{13}$$

$$T_* = \frac{\kappa[T(z_2) - T(z_1)]}{0.74[\ln\frac{z_2}{z_1} - \Psi_T(\xi_2) + \Psi_T(\xi_1)]} \tag{14}$$

where $U(z_1)$ and $U(z_2)$ are the measured velocities at heights z_1 and z_2, respectively, $T(z_1)$ and $T(z_2)$ are the measured temperatures at heights z_1 and z_2, respectively, ξ_1 and ξ_2 are the stabilities at heights z_1 and z_2, respectively, and Ψ_U and Ψ_T are the correction terms for the velocity and temperature profiles under the condition of stability L. Under unstable conditions (Stull, 1988), we have the following:

$$\Psi_U(\xi) = \ln[(\frac{1+x^2}{2})(\frac{1+x}{2})^2] - 2\arctan(x) + \frac{\pi}{2}, \quad x = (1-15\xi)^{1/4} \tag{15}$$

$$\Psi_T(\xi) = \ln[(\frac{1+y}{2})^2], \quad y = (1-9\xi)^{1/2} \tag{16}$$

Under stable conditions (Cheng and Brutsaert, 2005), we have the following:

$$\Psi_U(\xi) = -a\ln[\xi + (1+\xi^b)^{1/b}], \quad a=6.1, \ b=2.5. \tag{17}$$

$$\Psi_T(\xi) = -c\ln[\xi + (1+\xi^d)^{1/d}], \quad c=5.3, d=1.1. \tag{18}$$

Based on Eqs. (13)-(18), the friction velocity u_* and characteristic temperature T_* can be determined.

3 Measurements and data processing

3.1 Introduction of Experiments

Observations were collected at two locations (two rectangles in Fig. 1a) from December 2016 to March 2017: a rural site in Gucheng (GC site), Hebei Province and an urban site at the Chinese Academy of Meteorological Sciences (CAMS site) in Beijing. The distance between the two locations is approximately 100 km. According to the theoretical methods defined in the preceding section, to estimate the aerosol transport flux, the ratio of the aerosol mass to the imaginary part of the AERI, the ratio of the temperature to the real part of the AERI, the real and imaginary parts of the atmospheric equivalent refractive index structure parameter (AERISP), the friction speed, and the characteristic temperature must all be obtained. If the free convection condition is satisfied, fewer parameters are required, including the real and imaginary parts of the AERISP, the ratio of the aerosol mass to the imaginary part of the AERI, the ratio of the temperature to the real part of the AERI, and the atmospheric temperature.

Two sets of LASs developed by our research group were installed at the top of the building of the Beijing Institute of Meteorological Sciences (point A in Fig. 1b) and at the top of a two-story building in the farm of the Central Meteorological Bureau of Gucheng Town, Baoding City (point D in Fig. 1c). The light intensity sampling frequency of the receiving end was 500 Hz, and a file was recorded every 20 minutes. Then, the real and imaginary parts of the AERISP were calculated.

In the CAMS site, the transmitter end of the LAS was placed on the roof of a building on the east side of the Institute of Meteorological Sciences, and the receiver end was placed at the top of the Chinese Academy of Meteorological Sciences. The propagation path was along an east-west direction. The distance between the two ends was 550 metres as shown in Fig. 1d. The light beam

271 passed over urban buildings, residential areas and urban roads. The beam height was 43 metres. The

272 average height of the building below the beam was 24 metres; thus, the zero-displacement was 18

273 metres (24 * 0.67 = 18) (Leclerc and Foken, 2014), and the effective height of the beam was 25

274 metres. At the Beijing observation point, the temperature and wind speed of the near-surface

275 atmosphere were measured simultaneously, and the measurement heights were 1.5 m and 10 m,

276 respectively. To calculate the aerosol flux, it is necessary to obtain the ratio of the aerosol mass to

277 the imaginary part of AERI and to measure the aerosol mass concentration and visibility. In Haidian

278 District, there is a site to measure the visibility of the near-surface layer (point B in Fig. 1b), and the

279 PM_{10} mass concentration measurements were collected at Guanyuan Station (see point C in Fig.

280 1B). The sampling interval for the visibility and PM_{10} mass concentration measurements was 1 h.

281 The measurement height of points B and C in Fig. 1b was approximately 20 metres. The ratio of the

282 aerosol mass PM_{10} to the imaginary part of the AERI was calculated based on the data. The

283 measurements were collected at the CAMS site from January 15, 2017 to March 20, 2017.

284  In the GC site (point D in Fig. 1c, namely, the LAS position) in Gucheng, Baoding, Hebei, the

285 transmitter of the LAS was placed on the roof of a two-story building with a height of 8 m, and the

286 receiving end was located in a room in a three-story building on the west side of National Highway

287 107 at the same height as the transmitting end. The distance between the transmitting end and the

288 receiving end was 1670 metres. The terrain between the transmitting end and the receiving end was

289 flat, with farmland, a national road and sporadic trees below the beam, as seen in Fig. 1e. Near the

290 light beam, there was a 30-metre-high meteorological observation tower, in which the temperature,

291 relative humidity (RH), and wind speed were measured at 5 levels (1 m, 3 m, 8 m, 18 m, and 28 m).

292 The friction speed and characteristic temperature were calculated according to the temperature wind

293 speed profile. Visibility observations were made in Xushui District near the LAS position (see point

294 E in Fig. 1c). The PM_{10} mass concentration was measured in Beishi District (see point F in Fig. 1c).

295 From Fig. 1c, the three observation points (points D, E and F in Fig. 1c) formed a nearly straight

296 line and were distributed in a northeast-southwest direction. During the experimental observation

297 period, a northeast-southwest wind prevailed; thus, the Xushui District visibility data and Beishi

298 District PM_{10} data can approximate the situation of the scintillometer position. The measurements

299 were collected at the GC site from November 17, 2016 to March 30, 2017.

300 **3.2 Data quality control**

301  There are two types of variables, e.g., mean variables and fluctuation variables. Mean variables

302 include temperature, wind speed, wind direction, PM_{10}, and visibility for averages of 30 minutes or

303 60 minutes. Data quality control for the mean variables was conducted by comparing the measured

304 data at different heights or from personal experience. All the measured mean data were determined

305 to be adequate. Fluctuation variables include the high-frequency intensity fluctuation data measured

306 by the LAS, the real and imaginary parts of the AERISP, and the calculated aerosol flux. Quality

307 control mainly includes the elimination of spike and supplementing missing data.

308  Peaks in the light intensity fluctuation data appear because the received signal quickly increases

309 when the light signal is blocked, such as due to birds along the transmission path. This situation is

310 automatically determined by the data processing program. When this happens, the current 20-minute

311 period is rejected. For the real and imaginary parts of the AERISP and the aerosol flux data, (a) 3

312 times the standard deviation (SD) of the anomaly and (b) 3 times the SD of the adjacent difference

313   were determined. The method for judging 3 times the SD of the anomaly was applied to obtain a
314   trend of two-hour averages. Then, the difference between the measured value and the trend at each
315   moment was calculated, and the mean and SD of the difference were also calculated. The data with
316   differences from the trend exceeding 3 times the SD were considered as spikes. The method for
317   judging the difference of 3 times the SD of the adjacent differences was to first calculate the
318   difference between adjacent observations and then calculate the mean and SD of the difference. Any
319   data whose adjacent difference deviated from the mean of the adjacent difference by more than 3
320   the SD was considered an error. Less than 5% of the data were considered to contain spikes or errors.
321   The data determined to be errors were supplemented by the average of the nearby observations.
322   Of course, if data were missing over a long period, the missing gap could not be filled. For this
323   situation, further supplementation was not considered.
324   Other errors in the measurements using a LAS due to specific reasons (Moene et al., 2009); for
325   example, the impact of the uncertainty in the exact shape of the turbulence spectrum and the
326   intermittent variations in the characteristics of that spectrum on the LAS signal were not considered
327   in this study.

4 Results

329   First, the visibility and PM_{10} aerosol mass concentration results at the CAMS site and the GC
330   site are given and compared. Then, the characteristics of aerosol transport in typical weather
331   conditions at the CAMS site and the GC site are discussed. Finally, the aerosol flux characteristics
332   under heavy pollution weather conditions are analysed.

4.1 Relationship between n_{im} and PM_{10}

334   To obtain the ratio of the atmospheric aerosol mass concentration to the imaginary part of the
335   AERI (n_{im}) R_{MN}, PM_{10} and visibility were measured.
336   The maximum PM_{10} concentration in the Baoding area appeared at 1:00 on January 28, 2017
337   (up to 1071 µg m^{-3}), and the maximum PM_{10} concentration in the Beijing area appeared at 2:00 on
338   January 28, 2017 (up to 917 µg m^{-3}). This heavy pollution event swept through Beijing and the
339   surrounding areas, reaching a maximum at almost the same time. The visibility at the corresponding
340   time was less than 500 metres. The imaginary part of the AERI can be calculated from the visibility
341   (Yuan et al., 2016). Fig. 2a shows a scatter diagram of the imaginary parts of the AERI and PM_{10}
342   data measured in the Beijing area; there is a strong correlation between the AERI and aerosol particle
343   mass concentration, with a linear correlation coefficient of 0.96. The fitted linear in Fig. 2a has a
344   slope of 3845 kgm^{-3}. Therefore, R_{MN} was taken as 3845 kgm^{-3} for the Beijing area to estimate the
345   aerosol vertical transportation flux. Similarly, Fig. 2b shows the results for the Baoding area, and
346   R_{MN} was set to 3711 kgm^{-3} for the Baoding area to estimate the aerosol vertical transportation flux.
347   The two ratio coefficients are relatively close. Figs. 2a and 2b also show that in the case of light
348   pollution, Beijing's R_{MN} is slightly larger.
349   Furthermore, Figs. 2a and 2b show that although there is a large scattering between PM_{10} and
350   n_{IM} that may be attributed to a large separation between the two measurement locations for visibility
351   and PM_{10}, there is a strong linear correlation between the imaginary part of the AERI and PM_{10}. The
352   imaginary part of the AERI has a slightly stronger correlation with the PM_{10} data obtained in the
353   Baoding area than in the Beijing area.

354   The following provides the results of the aerosol transport flux under typical weather
355 conditions in Beijing and Baoding for the period from March 10, 2017 to March 17, 2017.

4.2 Characteristics of aerosol flux in the Beijing region

357   To analyse the aerosol transport flux characteristics, we present the time series of the
358 conventional meteorological parameters. The measurement site is the Beijing Meteorological
359 Observatory, which is 20 metres above the ground. The time series of temperature, RH, wind speed,
360 wind direction, PM_{10}, $C_{n,Re}^2$, $C_{n,Im}^2$ and aerosol flux are shown in Figs. 3a-3h, respectively. The
361 temperature has an obvious diurnal variation, indicating that this period had primarily sunny weather.
362 The RH from March 10, 2017 to March 17, 2017, was less than 60%, and the RH for most of the
363 time period was less than 30%. The wind speed was low; only during the period from March 11 to
364 March 14 was the wind strong. At 6:00 on March 12, the maximum wind speed was 4.2 m s^{-1}. At
365 that time, there was no dominant wind direction. Moreover, two light pollution events occurred
366 (MEP, 2012) on March 11 and March 16, with PM_{10} concentrations approaching 200 μgm^{-3}. From
367 the data of $C_{n,Re}^2$ and $C_{n,Im}^2$ in Figs. 3f and 3g, the real part of the AERISP $C_{n,Re}^2$ has obvious diurnal
368 variations, i.e., smaller in the morning and at night and larger at noon. The imaginary part of the
369 AERISP $C_{n,Im}^2$ had no obvious diurnal variation. According to Fig. 3g, there are some peak values,
370 i.e., some sudden increases and decreases, which may be related to sudden changes in wind direction,
371 as shown in Fig. 3d.

372   Aerosol fluxes in Beijing are calculated using the assumption of free convection. Because there
373 was no measurement of wind speed and temperature profiles near the LAS measurement location,
374 the friction velocity and characteristic temperature could not be calculated. Because the height of
375 the LAS instrument at the CAMS site was 43 m, the conditions assumed for free convection were
376 easily satisfied. During the day, the surface layer is usually unstable. At night, for the city, even if
377 there is an inversion at a higher altitude, due to the existence of the urban heat island, the surface
378 layer is often weakly unstable. The stable stratification situation is rare (Li et al., 2007).

379   From the aerosol flux time series given in Fig. 3h, the aerosol flux is large at noon and small
380 in the morning and at night, which is mainly because of the strong convection at noon. However,
381 large aerosol fluxes also occurred on the nights of March 11 and March 12, which were related to
382 high wind speeds. The mean aerosol flux measured at this observation point during this period was
383 0.0039 mgm^{-2}s^{-1}.

4.3 Characteristics of aerosol flux at the GC site

385   Similarly, Figs. 4a-4d provide the time series of temperature, RH, wind speed and wind
386 direction at 3 metres and 18 metres for the GC site, and Figs. 4e-4h show the PM_{10}, $C_{n,Re}^2$, $C_{n,Im}^2$
387 and aerosol flux curves over time. According to Fig. 4a, the temperatures at both heights show
388 obvious diurnal variations. The daytime is characterized by unstable stratification, and at night,
389 stable stratification prevails. Moreover, in the morning and evening, there is a transition period
390 between the stable and unstable stratification. Here, u_*, T_* and MO length L were calculated from
391 the wind speed and temperature measured at 3 m and 18 m on a meteorological tower. Fig. 4b shows
392 a plot of the two levels of RH over time, again with obvious diurnal variations. The RH of the GC
393 site was lower at the CAMS site. Figs. 4c and 4d provide the time series of wind speeds and wind

394   directions at two levels. At 6:00 on March 12, the wind speed was relatively high, and the maximum
395   at 18 metres was 6.5 m s^{-1}. At the same time, the maximum wind speed was reached in the Beijing
396   area, although the speed was lower in Beijing. The overall trend of wind direction at the GC site
397   was more consistent with the results of the CAMS site.

398   Figure 4e shows the PM$_{10}$ trend of over time. There were two light pollution events on March
399   11 and March 16. The overall trend is the same as in Fig. 3(e) except that there is a slight difference.
400   Figs. 4f and 4g show the time series of the imaginary and real parts of the AERISP for the GC site.
401   The real part of the AERISP is large at noon, and the optical turbulence is strong. The real part of
402   the AERISP is small during the morning and evening, and the corresponding turbulence is weak.
403   The imaginary part of the AERISP given in Fig. 4g does not show an obvious diurnal variation, and
404   there may be some sharp peaks.

405   Figure 4h shows the aerosol mass vertical flux changes over time. The aerosol flux has a
406   significant diurnal variation characteristic associated with turbulent transport near the surface. The
407   mean aerosol flux measured at the GC site during this period was 0.0016 mgm^{-2}s^{-1}. This value is
408   much smaller than the results for the CAMS site. Human activities contribute to increased water
409   vapor releases in urban areas compared to rural areas, as observed by Dou et al.(2014), and
410   especially for the night-time SBL in winter. During our observation period, the RH of the city was
411   lower than the rural area. However, human activities cause more aerosol particles in urban areas
412   than in rural areas.

413   **4.4 Aerosol flux during heavy pollution periods**

414   In the winter of 2016, there were several heavy pollution events. Generally, based on the PM$_{2.5}$
415   daily mean mass concentration limit in the primary standard of China's national environmental
416   quality standards (EPD, 2012), a pollution episode is referred to as the period during which the
417   PM$_{2.5}$ concentration exceeds 80 μg m^{-3} for 3 consecutive days between two clean periods, while a
418   period when the PM$_{2.5}$ level is less than 35 μg m^{-3} is defined as a clean period. Pollution episodes
419   with peak PM$_{2.5}$ values of more than 400 μg m^{-3} or less than 300 μg m^{-3} are termed heavy-pollution
420   episodes (HPEs) or light-pollution episodes (LPEs), respectively (Zhong et al., 2017).

421   A heavy pollution event began on December 1, 2016 and ended on January 10, 2017. Relevant
422   observational experiments were performed in the Beijing and Baoding areas, including observations
423   of meteorological parameters and aerosol parameters, to understand the causes of the heavy
424   pollution. The observations show that the beginning of the HPE was characterized by pollutant
425   transport under southerly conditions, i.e., the formation of heavy pollution was mainly caused by
426   the pollutants transported from southern Beijing, which we call the transport stage (TS). Usually,
427   after the TS stage, the explosive growth of PM$_{10}$ and the rapid accumulation of pollutants occur,
428   which is called the accumulative stage (AS). During the other period within the HPEs, aerosol
429   particles are usually removed from the atmosphere, which is called the removal stage (RS). During
430   heavy pollution events, there is a lower boundary layer depth, low wind speeds and high RH, and
431   the PM$_{10}$ concentration increases rapidly and reaches a very high value (Zhong et al., 2017). There
432   were 7 TS stages in the 2016 winter heavy pollution event, and the AS stage appeared immediately
433   after 4 TS stages. These included 00:00 on December 1 to 03:20 on December 4, 18:40 on December
434   15 to 00:00 on December 22, 00:00 on December 29 to January 2, and 00:00 and 8:40 on January 2
435   to 00:00 on January 5.

436   During this period, we used a LAS to conduct an observational study of the aerosol vertical
437   flux in the GC site, which was from 00:00 on December 1, 2016, to 00:00 on December 22, 2016.
438   No corresponding observations were made at the Beijing site during this period. Here, we first
439   discuss the observation results of the GC site, Baoding City, as shown in Fig. 5. Fig. 5a shows the
440   time series of the aerosol vertical transport flux. Figs. 5b-5g show the time series for the real and
441   imaginary parts of the AERISP, the temperature and RH at 18 metres, and the wind speed and
442   direction. Purple curves indicate the TS stages, red curves indicate the AS stages, and grey curves
443   indicate the RS stages.

444   According to Fig. 5a, in the TS stages and the RS stages, the aerosol flux exhibited diurnal
445   variations, while the AS stage did not show a diurnal variation. There were some peaks in the TS
446   stage. The average aerosol flux of the TS stages was 0.00065 $\mathrm{mgm^{-2}s^{-1}}$, the average value of the AS
447   stages was 0.00025 $\mathrm{mgm^{-2}s^{-1}}$, and the average value of the RS stages was 0.00063 $\mathrm{mgm^{-2}s^{-1}}$. The
448   aerosol transport fluxes in the TS and RS stages were similar, while the aerosol transport flux in the
449   AS stage was much smaller than the TS and RS stages.

450   According to Fig. 5b-5c, the imaginary structure parameters and the real structure parameters
451   of the refractive index in the TS and RS stages exhibited diurnal variations, while the AS stage did
452   not exhibit a diurnal variation. Fig. 5d shows that except for the second AS event (22:00 on
453   December 19, 2016 to 00:00, December 22, 2016), the temperature showed a diurnal variation.
454   During the AS stage, the RH (see Fig. 5e) was close to 100%, while the RH during the TS and RS
455   stages was lower. Moreover, Fig. 5f shows that during this time, the wind speed was relatively weak,
456   although the wind speed was slightly stronger on December 5. As shown in Fig. 5g, during the TS
457   and AS stages, southerly winds prevailed, while during the RS period, northerly winds prevailed.
458   The high wind speed and convection in the TS and RS stages contributed to the upward transport of
459   aerosol particles, whereas the low wind speed and stable stratification in the AS stage were not
460   conducive to the upward transport of aerosol particles.

461   During the heavy pollution period from December 1, 2016 to January 10, 2017, we did not
462   conduct surface aerosol flux observations at the CAMS site. From January 25 to January 31, the
463   pollution in the Beijing area also reached the level of heavy pollution. During this heavy pollution
464   period, a measurement of surface aerosol fluxes at the CAMS site was conducted. Figure 6 shows
465   the results of the meteorological and pollutant observations for 6 days from 00:00 on January 25,
466   2017 to 00:00 on January 31, 2017. According to Fig. 6, northerly winds prevailed after 12:00 on
467   January 26, when the concentration of PM_{10} dropped rapidly from 254 $\mu\mathrm{gm^{-3}}$ at 12:00 to 5 $\mu\mathrm{gm^{-3}}$ at
468   15:00. During the period 12:00-24:00 on January 26, the average wind speed was 2.6 $\mathrm{ms^{-1}}$. On
469   January 27, southerly winds prevailed, the average wind speed was only 0.8 $\mathrm{ms^{-1}}$, and the aerosol
470   concentration (PM_{10}) increased slowly; the increase began at 6:30 before increasing rapidly at 17:50,
471   reaching more than 300 $\mu\mathrm{gm^{-3}}$ at 23:00 and 917 $\mu\mathrm{gm^{-3}}$ at 2:00 am on January 28, which was the
472   maximum aerosol concentration over the 6 day period. Then, the aerosol concentration decreased
473   gradually. The average wind speed on January 27 was 0.6 $\mathrm{ms^{-1}}$, southerly winds prevailed, and the
474   mean PM_{10} concentration was 440 $\mu\mathrm{gm^{-3}}$, which constitutes a serious pollution level. The average
475   PM_{10} concentration during the period from 00:00 on January 25 to 00:00 on January 31 was 170
476     $\mu\mathrm{gm^{-3}}$.

477   According to the previous characteristics for the TS and AS stages, a period of southerly winds
478   can be determined as the TS stage. Thus, January 27 can be designated as the TS stage, January 28
479   can be determined as the AS stage, and January 29 can be determined as the RS stage. During

Beijing's heavy pollution event in January 2017 (20170125-20170131), the mean aerosol vertical flux in the TS stage was 0.0024 mgm^{-2}s^{-1}, the average value during the AS stage was 0.00087 mgm^{-2}s^{-1} and the RS stage was 0.0049 mgm^{-2}s^{-1}. The overall average value was 0.0032 mg m^{-2}s^{-1}.

Even during heavy pollution events, the RH in Beijing was lower than in the outer suburbs. According to Fig. 6e, the RH exceeded 60% in the period from 3:00 to 6:00 on January 26, where the maximum value was 63%, and the RH was less than 60% in the remaining periods. In urban areas, when the RH is low, heavy pollution incidents can occur. In Beijing, during the AS stage, the vertical flux of aerosol was less than during the TS and RS stages.

5 Discussions and conclusions

During the winter of 2016 and the spring of 2017, HPEs occurred frequently in the BTH area. This study investigated the aerosol vertical mass flux and compared its magnitude during different stages of HPEs, including RSs, TSs, and ASs, in two representative urban and rural sites, including the CAMS site in Beijing and the GC site in Hebei Province. Based on the light propagation theory and surface-layer similarity theory, the aerosol vertical mass flux was obtained by combining LAS observations, surface PM$_{2.5}$ and PM$_{10}$ mass concentrations, and meteorological observations, including air temperature and RH. We found that under favourable meteorological conditions for pollution dispersion, i.e., from March 10, 2017 to March 17, 2017, the vertical aerosol mass flux exhibited striking diurnal variations, with the mass fluxes reaching peak values at noon and lowering in the morning and evening. During the HPEs from January 25, 2017 to January 31, 2017 in Beijing, the vertical aerosol mass flux varied substantially during the different stages. Specifically, the mean mass flux decreased by 51% from 0.0049 mg m^{-2}s^{-1} in the RSs to 0.0024 mg m^{-2}s^{-1} in the TSs, which was partly due to the wind speed reduction from strong northerly winds in the RSs to southerly winds in the TSs. During the ASs, the mean mass flux decreased further to 0.00087 mg m^{-2}s^{-1}, which accounted for approximately 1/3 of the flux during the TSs. Due to the cooling effect of elevated aerosols in the ASs, the near-ground temperature decreased and caused or reinforced the inversion, which suppressed the turbulence diffusion. The weakened mass flux would further facilitate aerosol accumulation. During the HPE from December 01, 2016, to December 22, 2016, in Gucheng, the mean mass flux was similar in the RSs and TSs, ranging from 0.00063 mg m^{-2}s^{-1} to 0.00065 mg m^{-2}s^{-1}. This is partly because Gucheng was less affected by strong northerly winds than Beijing. Thus, the wind speed varied slightly from the RSs to TSs. However, the mass flux decreased substantially to 0.00025 mg m^{-2}s^{-1} in the ASs, which was merely 1/3 of the mean flux in the TSs.

In this study, the aerosol emission flux was also estimated in these two rural and urban sites. Generally, compared with the emissions in spring, we found that in winter, the near-ground emissions were weaker in suburban areas and were similar in urban areas. In suburban areas, although the aerosol concentrations were relatively high (Shen et al., 2018), the upward emitted aerosol flux was smaller than in urban areas. During the ASs of the HPEs, the aerosol emission flux from the ground was weaker than for the RSs and TSs at both the CAMS and GC sites, which indicates that surface pollutant emissions are not the major cause of explosive PM$_{2.5}$ growth. During the ASs with weak solar radiation, the factors most associated with aerosol concentration changes were horizontal transport and BL height variations, which might be the main causes of increased PM$_{2.5}$ (Zhong et al., 2018b;Zhong et al., 2018a;Zhang et al., 2018).

Due to the lack of necessary experimental conditions, such as meteorological towers and EC systems, current experimental results cannot be compared with EC methods. According to the

523 literature data, the two methods have been compared indirectly, and the estimated aerosol flux under
524 different measurement conditions is consistent in magnitude (Yuan et al., 2016). However, a direct
525 comparison of the two methods is in development.
526 Compared with the EC method, the aerosol flux has high spatial representativeness based on
527 the principle of light propagation, and there is no need to install a high tower. However, the
528 estimation of aerosol fluxes using the LAS method still has theoretical and practical deficiencies.
529 At present, the LAS method for the aerosol flux regards the aerosol particles as ordinary scalar
530 molecules. At the same time, based on the assumption of the equivalent medium, the imaginary part
531 of the AERI is taken for granted as proportional to the aerosol mass concentration. This is often not
532 the case. The actual turbulence spectrum shape often deviates from the "-5/3" law, and turbulence
533 intermittent and scintillation saturation can also occur (Moene et al., 2009). The applicability of the
534 near-surface layer similarity theory to the aerosol particle motion under stable layer conditions also
535 has many problems. The formation of new particles and changes in aerosol particle size distribution
536 also affect the scintillation in light propagation. There are also practical problems such as untimely
537 maintenance, rainfall and low visibility, and platform vibrations required for observation. All these
538 problems will cause errors in final estimates, so more theoretical and experimental research is
539 needed.
540

541 **Author contributions**. Renmin Yuan and Xiaoye Zhang designed experiments and wrote the manuscript;
542 Renmin Yuan, Hao Liu, Yu Gui, Bohao Shao, Yaqiang Wang, Junting Zhong and Xaioping Tao
543 carried out experiments; Renmin Yuan analyzed experimental results. Yubin Li and Zhiqiu Gao
544 designed experiments and discussed the results.
545

546 **Acknowledgements**. This study was supported by the National Key Research and Development Program
547 under grant no. 2016YFC0203306 and the National Natural Science Foundation of China
548 (41775014, 51677175).

References

550 Ahlm, L., Krejci, R., Nilsson, E. D., Martensson, E. M., Vogt, M., and Artaxo, P.: Emission and dry deposition of
551 accumulation mode particles in the Amazon Basin, Atmospheric Chemistry And Physics, 10, 10237-10253,
552 10.5194/acp-10-10237-2010, 2010a.
553 Ahlm, L., Nilsson, E. D., Krejci, R., Martensson, E. M., Vogt, M., and Artaxo, P.: A comparison of dry and wet
554 season aerosol number fluxes over the Amazon rain forest, Atmospheric Chemistry And Physics, 10, 3063-
555 3079, 10.5194/acp-10-3063-2010, 2010b.
556 Akagi, S. K., Yokelson, R. J., Wiedinmyer, C., Alvarado, M. J., Reid, J. S., Karl, T., Crounse, J. D., and Wennberg,
557 P. O.: Emission factors for open and domestic biomass burning for use in atmospheric models, Atmospheric
558 Chemistry And Physics, 11, 4039-4072, 10.5194/acp-11-4039-2011, 2011.
559 Bond, T. C., Streets, D. G., Yarber, K. F., Nelson, S. M., Woo, J. H., and Klimont, Z.: A technology-based global
560 inventory of black and organic carbon emissions from combustion, Journal Of Geophysical Research-
561 Atmospheres, 109, 10.1029/2003jd003697, 2004.
562 Brooks, I. M., Yelland, M. J., Upstill-Goddard, R. C., Nightingale, P. D., Archer, S., d'Asaro, E., Beale, R., Beatty,
563 C., Blomquist, B., Bloom, A. A., Brooks, B. J., Cluderay, J., Coles, D., Dacey, J., DeGrandpre, M., Dixon, J.,
564 Drennan, W. M., Gabriele, J., Goldson, L., Hardman-Mountford, N., Hill, M. K., Horn, M., Hsueh, P.-C.,
565 Huebert, B., de Leeuw, G., Leighton, T. G., Liddicoat, M., Lingard, J. J. N., McNeil, C., McQuaid, J. B., Moat,

566   B. I., Moore, G., Neill, C., Norris, S. J., O'Doherty, S., Pascal, R. W., Prytherch, J., Rebozo, M., Sahlee, E.,
567   Salter, M., Schuster, U., Skjelvan, I., Slagter, H., Smith, M. H., Smith, P. D., Srokosz, M., Stephens, J. A.,
568   Taylor, P. K., Telszewski, M., Walsh, R., Ward, B., Woolf, D. K., Young, D., and Zemmelink, H.: Physical
569   exchanges at the air-sea interface uk-solas field measurements, Bulletin of the American Meteorological
570   Society, 90, 629-+, 10.1175/2008bams2578.1, 2009.
571   Cao, J., Xu, H., Xu, Q., Chen, B., and Kan, H.: Fine Particulate Matter Constituents and Cardiopulmonary Mortality
572   in a Heavily Polluted Chinese City, Environmental Health Perspectives, 120, 373-378, 10.1289/ehp.1103671,
573   2012.
574   Ceburnis, D., Rinaldi, M., Ovadnevaite, J., Martucci, G., Giulianelli, L., and O'Dowd, C. D.: Marine submicron
575   aerosol gradients, sources and sinks, Atmospheric Chemistry and Physics, 16, 12425-12439, 10.5194/acp-16-
576   12425-2016, 2016.
577   Chen, Y., Tian, C., Feng, Y., Zhi, G., Li, J., and Zhang, G.: Measurements of emission factors of PM2.5, OC, EC,
578   and BC for household stoves of coal combustion in China, Atmospheric Environment, 109, 190-196,
579   10.1016/j.atmosenv.2015.03.023, 2015.
580   Cheng, Y. G., and Brutsaert, W.: Flux-profile relationships for wind speed and temperature in the stable atmospheric
581   boundary layer, Boundary-Layer Meteorology, 114, 519-538, 10.1007/s10546-004-1425-4, 2005.
582   DeBruin, H. A. R., vandenHurk, B., and Kohsiek, W.: The scintillation method tested over a dry vineyard area,
583   Boundary-Layer Meteorology, 76, 25-40, 1995.
584   Dou, J., Wang, Y., and Miao, S.: Fine Spatial and Temporal Characteristics of Humidity and Wind in Beijing Urban
585   Area, Journal of Applied Meteorological Science, 25, 559-569, 2014.
586   Dubovik, O., Holben, B., Eck, T. F., Smirnov, A., Kaufman, Y. J., King, M. D., Tanre, D., and Slutsker, I.: Variability
587   of absorption and optical properties of key aerosol types observed in worldwide locations, J. Atmos. Sci., 59,
588   590-608, 10.1175/1520-0469(2002)059<0590:voaaop>2.0.co;2, 2002.
589   Elbert, W., Taylor, P. E., Andreae, M. O., and Poeschl, U.: Contribution of fungi to primary biogenic aerosols in the
590   atmosphere: wet and dry discharged spores, carbohydrates, and inorganic ions, Atmospheric Chemistry and
591   Physics, 7, 4569-4588, 10.5194/acp-7-4569-2007, 2007.
592   EPD, E. P. D.: Technical regulation on ambient air quality index (on trial), Beijing, 12 pp., 2012.
593   Evans, J. G., and De Bruin, H. A. R.: The Effective Height of a Two-Wavelength Scintillometer System, Bound-Lay.
594   Meteorol., 141, 165-177, 10.1007/s10546-011-9634-0, 2011.
595   Farmer, D. K., Kimmel, J. R., Phillips, G., Docherty, K. S., Worsnop, D. R., Sueper, D., Nemitz, E., and Jimenez, J.
596   L.: Eddy covariance measurements with high-resolution time-of-flight aerosol mass spectrometry: a new
597   approach to chemically resolved aerosol fluxes, Atmos. Meas. Tech., 4, 1275-1289, 10.5194/amt-4-1275-2011,
598   2011.
599   Gordon, M., Staebler, R. M., Liggio, J., Vlasenko, A., Li, S.-M., and Hayden, K.: Aerosol flux measurements above
600   a mixed forest at Borden, Ontario Atmos. Chem. Phys., 11, 6773-6786, 2011.
601   Graham, B., Guyon, P., Taylor, P. E., Artaxo, P., Maenhaut, W., Glovsky, M. M., Flagan, R. C., and Andreae, M. O.:
602   Organic compounds present in the natural Amazonian aerosol: Characterization by gas chromatography-mass
603   spectrometry, Journal Of Geophysical Research-Atmospheres, 108, 10.1029/2003jd003990, 2003.
604   Guo, H., Xu, M., and Hu, Q.: Changes in near-surface wind speed in China: 1969-2005, International Journal Of
605   Climatology, 31, 349-358, 10.1002/joc.2091, 2011.
606   Harrison, R. M., Dall'Osto, M., Beddows, D. C. S., Thorpe, A. J., Bloss, W. J., Allan, J. D., Coe, H., Dorsey, J. R.,
607   Gallagher, M., Martin, C., Whitehead, J., Williams, P. I., Jones, R. L., Langridge, J. M., Benton, A. K., Ball, S.
608   M., Langford, B., Hewitt, C. N., Davison, B., Martin, D., Petersson, K. F., Henshaw, S. J., White, I. R.,
609   Shallcross, D. E., Barlow, J. F., Dunbar, T., Davies, F., Nemitz, E., Phillips, G. J., Helfter, C., Di Marco, C. F.,

610 and Smith, S.: Atmospheric chemistry and physics in the atmosphere of a developed megacity (London): an
611   overview of the REPARTEE experiment and its conclusions, , Atmos. Chem. Phys., 12, 3065-3114,
612   10.5194/acp-12-3065-2012, 2012, 2012.

613 Hartogensis, O. K., Watts, C. J., Rodriguez, J. C., and De Bruin, H. A. R.: Derivation of an effective height for
614   scintillometers: La Poza experiment in Northwest Mexico, Journal of Hydrometeorology, 4, 915-928,
615   10.1175/1525-7541(2003)004<0915:doaehf>2.0.co;2, 2003.

616 He, Y., Gao, Z., Guo, T., Qu, F., Liang, D., Li, D., Shi, J., and Shan, B.: Fine particulate matter associated mortality
617   burden of lung cancer in Hebei Province, China, Thoracic Cancer, 9, 820-826, 10.1111/1759-7714.12653, 2018.

618 Hourdin, F., Gueye, M., Diallo, B., Dufresne, J. L., Escribano, J., Menut, L., Marticorena, B., Siour, G., and Guichard,
619   F.: Parameterization of convective transport in the boundary layer and its impact on the representation of the
620   diurnal cycle of wind and dust emissions, Atmospheric Chemistry and Physics, 15, 6775-6788, 10.5194/acp-
621   15-6775-2015, 2015.

622 Huang, R.-J., Zhang, Y., Bozzetti, C., Ho, K.-F., Cao, J.-J., Han, Y., Daellenbach, K. R., Slowik, J. G., Platt, S. M.,
623   Canonaco, F., Zotter, P., Wolf, R., Pieber, S. M., Bruns, E. A., Crippa, M., Ciarelli, G., Piazzalunga, A.,
624   Schwikowski, M., Abbaszade, G., Schnelle-Kreis, J., Zimmermann, R., An, Z., Szidat, S., Baltensperger, U.,
625   El Haddad, I., and Prevot, A. S. H.: High secondary aerosol contribution to particulate pollution during haze
626   events in China, Nature, 514, 218-222, 10.1038/nature13774, 2014.

627 Jarvi, L., Rannik, U., Mammarella, I., Sogachev, A., Aalto, P. P., Keronen, P., Siivola, E., Kulmala, M., and Vesala,
628   T.: Annual particle flux observations over a heterogeneous urban area, Atmos. Chem. Phys., 9, 7847-7856,
629   2009.

630 Kaimal, J. C., Izumi, Y., Wyngaard, J. C., and Cote, R.: Spectral characteristics of surface-layer turbulence, Q. J.
631   Roy. Meteor. Soc., 98, 563-589, 1972.

632 Karvosenoja, N., Tainio, M., Kupiainen, K., Tuomisto, J. T., Kukkonen, J., and Johansson, M.: Evaluation of the
633   emissions and uncertainties of PM2.5 originated from vehicular traffic and domestic wood combustion in
634   Finland, Boreal Environment Research, 13, 465-474, 2008.

635 Ketzel, M., Wahlin, P., Berkowicz, R., and Palmgren, F.: Particle and trace gas emission factors under urban driving
636   conditions in Copenhagen based on street and roof-level observations, Atmospheric Environment, 37, 2735-
637   2749, 10.1016/s1352-2310(03)00245-0, 2003.

638 Krecl, P., Targino, A. C., Landi, T. P., and Ketzel, M.: Determination of black carbon, PM2.5, particle number and
639   NOx emission factors from roadside measurements and their implications for emission inventory development,
640   Atmospheric Environment, 186, 229-240, 10.1016/j.atmosenv.2018.05.042, 2018.

641 Lagouarde, J. P., Irvine, M., Bonnefond, J. M., Grimmond, C. S. B., Long, N., Oke, T. R., Salmond, J. A., and Offerle,
642   B.: Monitoring the sensible heat flux over urban areas using large aperture scintillometry: Case study of
643   Marseille city during the escompte experiment, Boundary-Layer Meteorology, 118, 449-476, 10.1007/s10546-
644   005-9001-0, 2006.

645 Leclerc, M. Y., and Foken, T.: Footprints in Micrometeorology and Ecology, Spinger, Heidelberg, 254 pp., 2014.

646 Lee, X.: Handbook of Micrometeorology,A Guide for Surface Flux Measurement and Analysis, edited by: Lee, X.,
647   Kluwer academic publishers, New York, USA, 250 pp., 2004.

648 Lei, H., and Wuebbles, D. J.: Chemical competition in nitrate and sulfate formations and its effect on air quality,
649   Atmospheric Environment, 80, 472-477, 10.1016/j.atmosenv.2013.08.036, 2013.

650 Li, J., Sun, J., Zhou, M., Cheng, Z., Li, Q., Cao, X., and Zhang, J.: Observational analyses of dramatic developments
651   of a severe air pollution event in the Beijing area, Atmospheric Chemistry and Physics, 18, 3919-3935,
652   10.5194/acp-18-3919-2018, 2018.

653 Li, X., Hu, F., and Shu, W.: Study on the characteristics of winter island heat islands in Beijing and the influence

654   factors of strong and weak heat islands, Journal of the Graduate School of the Chinese Academy of Sciences,
655   4, 431-438, 2007.
656 Liu, H., Man, H., Cui, H., Wang, Y., Deng, F., Wang, Y., Yang, X., Xiao, Q., Zhang, Q., Ding, Y., and He, K.: An
657   updated emission inventory of vehicular VOCs and IVOCs in China, Atmospheric Chemistry And Physics, 17,
658   12709-12724, 10.5194/acp-17-12709-2017, 2017.
659 Lu, Z., Zhang, Q., and Streets, D. G.: Sulfur dioxide and primary carbonaceous aerosol emissions in China and India,
660   1996-2010, Atmospheric Chemistry And Physics, 11, 9839-9864, 10.5194/acp-11-9839-2011, 2011.
661 Martensson, E. M., Nilsson, E. D., Buzorius, G., and Johansson, C.: Eddy covariance measurements and
662   parameterisation of traffic related particle emissions in an urban environment, Atmos. Chem. Phys., 6, 769-
663   785, 2006.
664 Mayol, E., Jimenez, M. A., Herndl, G. J., Duarte, C. M., and Arrieta, J. M.: Resolving the abundance and air-sea
665   fluxes of airborne microorganisms in the North Atlantic Ocean, Frontiers in Microbiology, 5,
666   10.3389/fmicb.2014.00557, 2014.
667 MEP, P. R. C.: Technical regulation on ambient air quality index, Ministry of Environmental Protection, Beijing, 12
668   pp., 2012.
669 Moene, A. F., Beyrich, F., and Hartogensis, O. K.: Developments in scintillometry, Bulletin of the American
670   Meteorological Society, 90, 694-698, 10.1175/2008bams2672.1, 2009.
671 Nemitz, E., Dorsey, J. R., Flynn, M. J., Gallagher, M. W., Hensen, A., Erisman, J.-W., Owen, S. M., ammgen, U. D.,
672   and Sutton, M. A.: Aerosol fluxes and particle growth above managed grassland, Biogeosciences, 6, 1627-
673   1645, 2009.
674 Ripamonti, G., Jarvi, L., Molgaard, B., Hussein, T., Nordbo, A., and Hameri, K.: The effect of local sources on
675   aerosol particle number size distribution, concentrations and fluxes in Helsinki, Finland, Tellus B., 65,
676   10.3402/tellusb.v65i0.19786, 2013.
677 Roden, C. A., Bond, T. C., Conway, S., Benjamin, A., and Pinel, O.: Emission factors and real-time optical properties
678   of particles emitted from traditional wood burning cookstoves, Environmental Science & Technology, 40,
679   6750-6757, 10.1021/es052080i, 2006.
680 Shen, G., Tao, S., Wei, S., Chen, Y., Zhang, Y., Shen, H., Huang, Y., Zhu, D., Yuan, C., Wang, H., Wang, Y., Pei, L.,
681   Liao, Y., Duan, Y., Wang, B., Wang, R., Lv, Y., Li, W., Wang, X., and Zheng, X.: Field Measurement of
682   Emission Factors of PM, EC, OC, Parent, Nitro-, and Oxy- Polycyclic Aromatic Hydrocarbons for Residential
683   Briquette, Coal Cake, and Wood in Rural Shanxi, China, Environmental Science & Technology, 47, 2998-
684   3005, 10.1021/es304599g, 2013.
685 Shen, X., Sun, J., Zhang, X., Zhang, Y., Wang, Y., Tan, K., Wang, P., Zhang, L., Qi, X., Che, H., Zhang, Z., Zhong,
686   J., Zhao, H., and Ren, S.: Comparison of Submicron Particles at a Rural and an Urban Site in the North China
687   Plain during the December 2016 Heavy Pollution Episodes, Journal of Meteorological Research, 32, 26-37,
688   10.1007/s13351-018-7060-7, 2018.
689 Sproson, D. A. J., Brooks, I. M., and Norris, S. J.: The effect of hygroscopicity on eddy covariance estimates of sea-
690   spray aerosol fluxes: a comparison of high-rate and bulk correction methods, Atmos. Meas. Tech., 6, 323-335,
691   2013.
692 Stull, R. B.: An Introduction to Boundary Layer Meteorology, Reidel Publishing Co., Dordrecht, 666 pp., 1988.
693 Sun, Y., Jiang, Q., Wang, Z., Fu, P., Li, J., Yang, T., and Yin, Y.: Investigation of the sources and evolution processes
694   of severe haze pollution in Beijing in January 2013, Journal Of Geophysical Research-Atmospheres, 119,
695   4380-4398, 10.1002/2014jd021641, 2014.
696 Tatarskii, V. I.: Wave Propagation in a Turbulent Medium, McGraw-Hill Book Company Inc., New York, 285 pp.,
697   1961.

698 Vogt, M., Nilsson, E. D., Ahlm, L., Martensson, E. M., and Johansson, C.: Seasonal and diurnal cycles of 0.25-2.5
699   mu m aerosol fluxes over urban Stockholm, Sweden, Tellus B., 63, 935-951, 10.1111/j.1600-
700   0889.2011.00551.x, 2011a.

701 Vogt, M., Nilsson, E. D., Ahlm, L., Martensson, E. M., and Johansson, C.: The relationship between 0.25-2.5 mu m
702   aerosol and CO2 emissions over a city, Atmos. Chem. Phys., 11, 4851-4859, 10.5194/acp-11-4851-2011,
703   2011b.

704 Wang, H., Lu, K., Chen, X., Zhu, Q., Wu, Z., Wu, Y., and Sun, K.: Fast particulate nitrate formation via N2O5 uptake
705   aloft in winter in Beijing, Atmospheric Chemistry and Physics, 18, 10483-10495, 10.5194/acp-18-10483-2018,
706   2018.

707 Wang, Y. H., Liu, Z. R., Zhang, J. K., Hu, B., Ji, D. S., Yu, Y. C., and Wang, Y. S.: Aerosol physicochemical properties
708   and implications for visibility during an intense haze episode during winter in Beijing, Atmospheric Chemistry
709   And Physics, 15, 3205-3215, 10.5194/acp-15-3205-2015, 2015.

710 Wang, Z., Li, J., Wang, Z., Yang, W., Tang, X., Ge, B., Yan, P., Zhu, L., Chen, X., Chen, H., Wand, W., Li, J., Liu,
711   B., Wang, X., Wand, W., Zhao, Y., Lu, N., and Su, D.: Modeling study of regional severe hazes over mid-
712   eastern China in January 2013 and its implications on pollution prevention and control, Science China-Earth
713   Sciences, 57, 3-13, 10.1007/s11430-013-4793-0, 2014.

714 Whitehead, J. D., Gallagher, M. W., Dorsey, J. R., Robinson, N., Gabey, A. M., Coe, H., McFiggans, G., Flynn, M.
715   J., Ryder, J., Nemitz, E., and Davies, F.: Aerosol fluxes and dynamics within and above a tropical rainforest in
716   South-East Asia, Atmospheric Chemistry And Physics, 10, 9369-9382, 10.5194/acp-10-9369-2010, 2010.

717 Wu, Q., Wang, Z., Chen, H., Zhou, W., and Wenig, M.: An evaluation of air quality modeling over the Pearl River
718   Delta during November 2006, Meteorology And Atmospheric Physics, 116, 113-132, 10.1007/s00703-011-
719   0179-z, 2012.

720 Wyngaard, J. C., Izumi, Y., and Collins, S. A.: Behavior of refractive-index-structure parameter near ground, J. Opt.
721   Soc. Am., 61, 1646-1650, 10.1364/josa.61.001646, 1971.

722 Wyngaard, J. C.: Turbulence in the Atmosphere, Cambridge University Press, New York, 393 pp., 2010.

723 Yuan, R., Luo, T., Sun, J., Zeng, Z., Ge, C., and Fu, Y.: A new method for measuring the imaginary part of the
724   atmospheric refractive index structure parameter in the urban surface layer, Atmospheric Chemistry and
725   Physics, 15, 2521-2531, 10.5194/acp-15-2521-2015, 2015.

726 Yuan, R., Luo, T., Sun, J., Liu, H., Fu, Y., and Wang, Z.: A new method for estimating aerosol mass flux in the urban
727   surface layer using LAS technology, Atmospheric Measurement Techniques, 9, 1925-1937, 10.5194/amt-9-
728   1925-2016, 2016.

729 Zeweldi, D. A., Gebremichael, M., Wang, J., Sammis, T., Kleissl, J., and Miller, D.: Intercomparison of Sensible
730   Heat Flux from Large Aperture Scintillometer and Eddy Covariance Methods: Field Experiment over a
731   Homogeneous Semi-arid Region, Bound-Lay. Meteorol., 135, 151-159, 10.1007/s10546-009-9460-9, 2010.

732 Zhang, H., and Li, X.: Review of the field measurements and parameterization for dust emission during sand-dust
733   events, Journal of Meteorological Research, 28, 903-922, 10.1007/s13351-014-3296-z, 2014.

734 Zhang, Q., Streets, D. G., Carmichael, G. R., He, K. B., Huo, H., Kannari, A., Klimont, Z., Park, I. S., Reddy, S., Fu,
735   J. S., Chen, D., Duan, L., Lei, Y., Wang, L. T., and Yao, Z. L.: Asian emissions in 2006 for the NASA INTEX-
736   B mission, Atmospheric Chemistry And Physics, 9, 5131-5153, 10.5194/acp-9-5131-2009, 2009a.

737 Zhang, X., Zhong, J., Wang, J., Wang, Y., and Liu, Y.: The interdecadal worsening of weather conditions affecting
738   aerosol pollution in the Beijing area in relation to climate warming, Atmospheric Chemistry and Physics, 18,
739   5991-5999, 10.5194/acp-18-5991-2018, 2018.

740 Zhang, X. Y., Wang, Y. Q., Lin, W. L., Zhang, Y. M., Zhang, X. C., Gong, S., Zhao, P., Yang, Y. Q., Wang, J. Z., Hou,
741   Q., Zhang, X. L., Che, H. Z., Guo, J. P., and Li, Y.: CHANGES OF ATMOSPHERIC COMPOSITION AND

742   OPTICAL PROPERTIES OVER BEIJING 2008 Olympic Monitoring Campaign, Bulletin Of the American
743   Meteorological Society, 90, 1633-+, 10.1175/2009bams2804.1, 2009b.
744   Zhang, X. Y., Wang, Y. Q., Niu, T., Zhang, X. C., Gong, S. L., Zhang, Y. M., and Sun, J. Y.: Atmospheric aerosol
745   compositions in China: spatial/temporal variability, chemical signature, regional haze distribution and
746   comparisons with global aerosols, Atmospheric Chemistry And Physics, 12, 779-799, 10.5194/acp-12-779-
747   2012, 2012.
748   Zhang, Y., and Tao, S.: Global atmospheric emission inventory of polycyclic aromatic hydrocarbons (PAHs) for
749   2004, Atmospheric Environment, 43, 812-819, 10.1016/j.atmosenv.2008.10.050, 2009.
750   Zheng, B., Zhang, Q., Tong, D., Chen, C., Hong, C., Li, M., Geng, G., Lei, Y., Huo, H., and He, K.: Resolution
751   dependence of uncertainties in gridded emission inventories: a case study in Hebei, China, Atmospheric
752   Chemistry And Physics, 17, 921-933, 10.5194/acp-17-921-2017, 2017.
753   Zhong, J., Zhang, X., Wang, Y., Sun, J., Zhang, Y., Wang, J., Tan, K., Shen, X., Che, H., Zhang, L., Zhang, Z., Qi,
754   X., Zhao, H., Ren, S., and Li, Y.: Relative Contributions of Boundary-Layer Meteorological Factors to the
755   Explosive Growth of PM2.5 during the Red-Alert Heavy Pollution Episodes in Beijing in December 2016,
756   Journal Of Meteorological Research, 31, 809-819, 10.1007/s13351-017-7088-0, 2017.
757   Zhong, J., Zhang, X., Dong, Y., Wang, Y., Liu, C., Wang, J., Zhang, Y., and Che, H.: Feedback effects of boundary-
758   layer meteorological factors on cumulative explosive growth of PM2.5 during winter heavy pollution episodes
759   in Beijing from 2013 to 2016, Atmospheric Chemistry And Physics, 18, 247-258, 10.5194/acp-18-247-2018,
760   2018a.
761   Zhong, J., Zhang, X., Wang, Y., Liu, C., and Dong, Y.: Heavy aerosol pollution episodes in winter Beijing enhanced
762   by radiative cooling effects of aerosols, Atmospheric Research, 209, 59-64, 10.1016/j.atmosres.2018.03.011,
763   2018b.

764

765
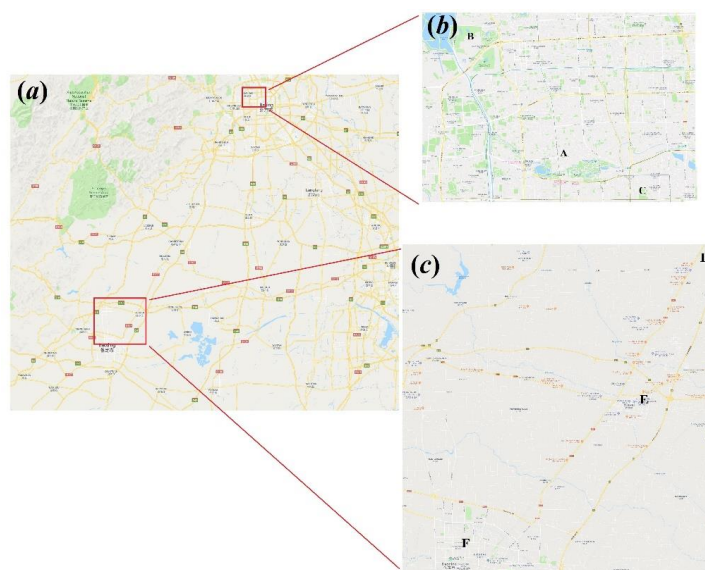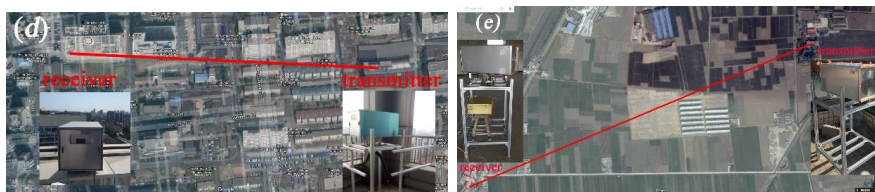
Figure 1. Photographs of the measurement site. (a) Map of the experiment area in the Beijing urban area and suburban area and (b) expanded view of the Beijing experiment area, which is marked as the shaded rectangle in (a). (c) Expanded view of the Baoding experiment area, which is marked as the shaded rectangle in (a). (d) Satellite image of the CAMS site and (e) the satellite image of the GC site. Figs. 1a, b, c, and d © Google.
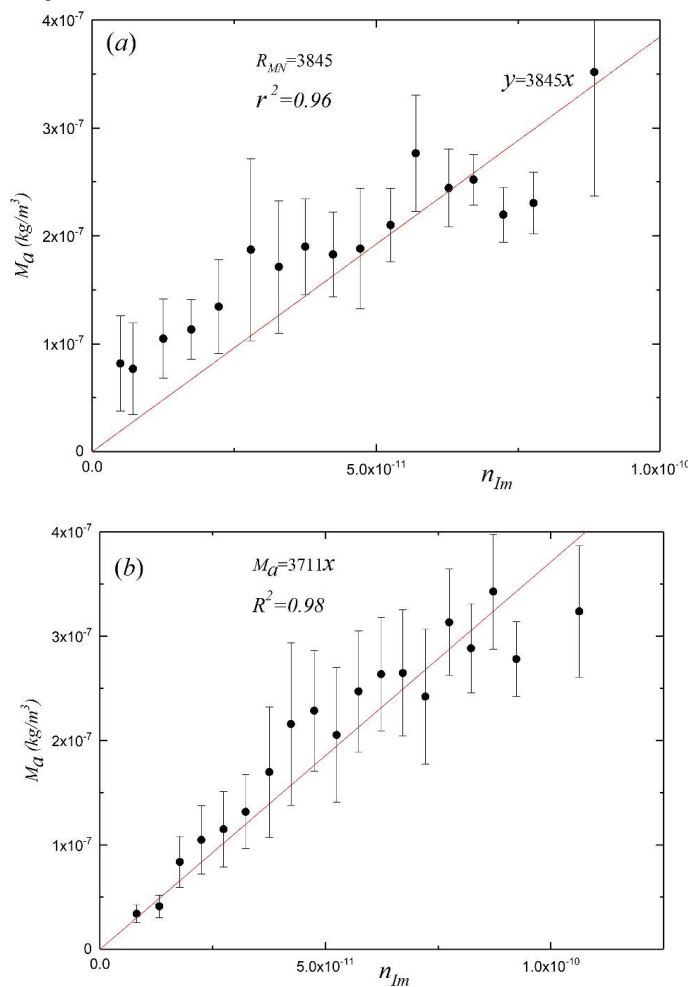
Figure 2. Scatterplots of aerosol mass concentration M_a vs. the imaginary part of the AERI for (a) the Beijing area and (b) the Baoding area.

777

778
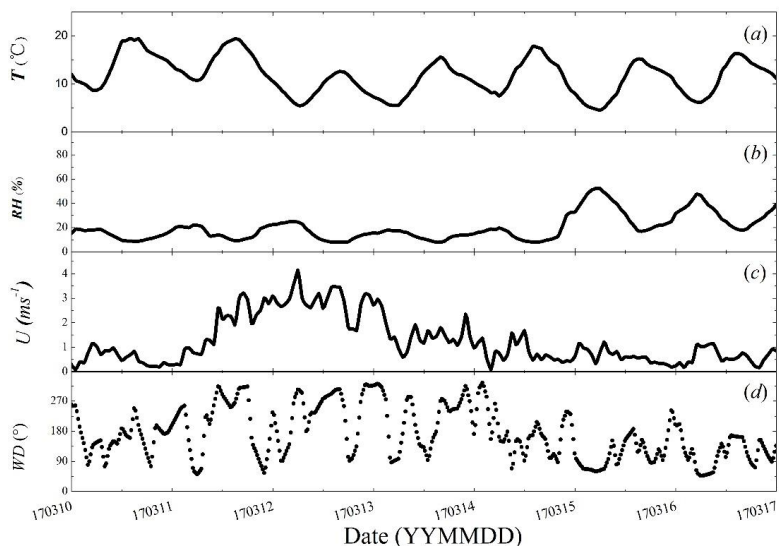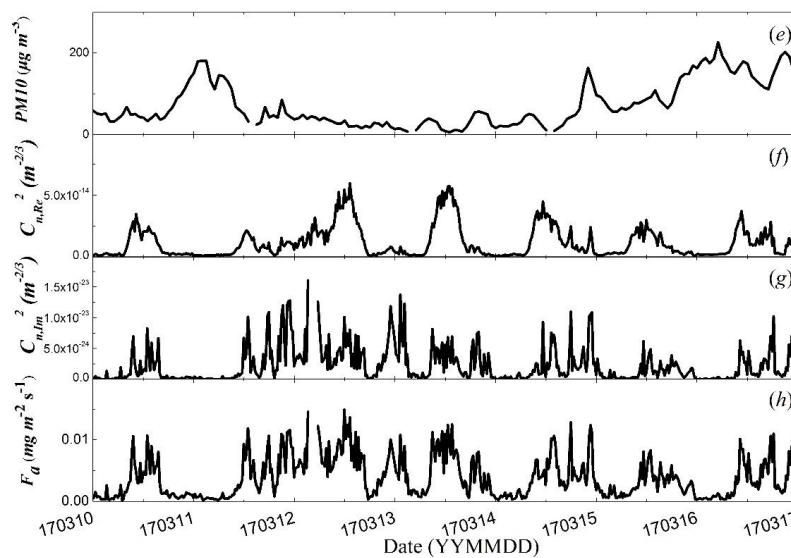
Figure 3. Temporal variations in (a) air temperature, (b) RH, (c) wind speed, (d) wind direction, (e) PM$_{10}$,
(f) real part of the AERISP, (g) imaginary part of the AERISP and (h) aerosol mass flux in the Beijing
area from March 10, 2017 to March 17, 2017.

782

783
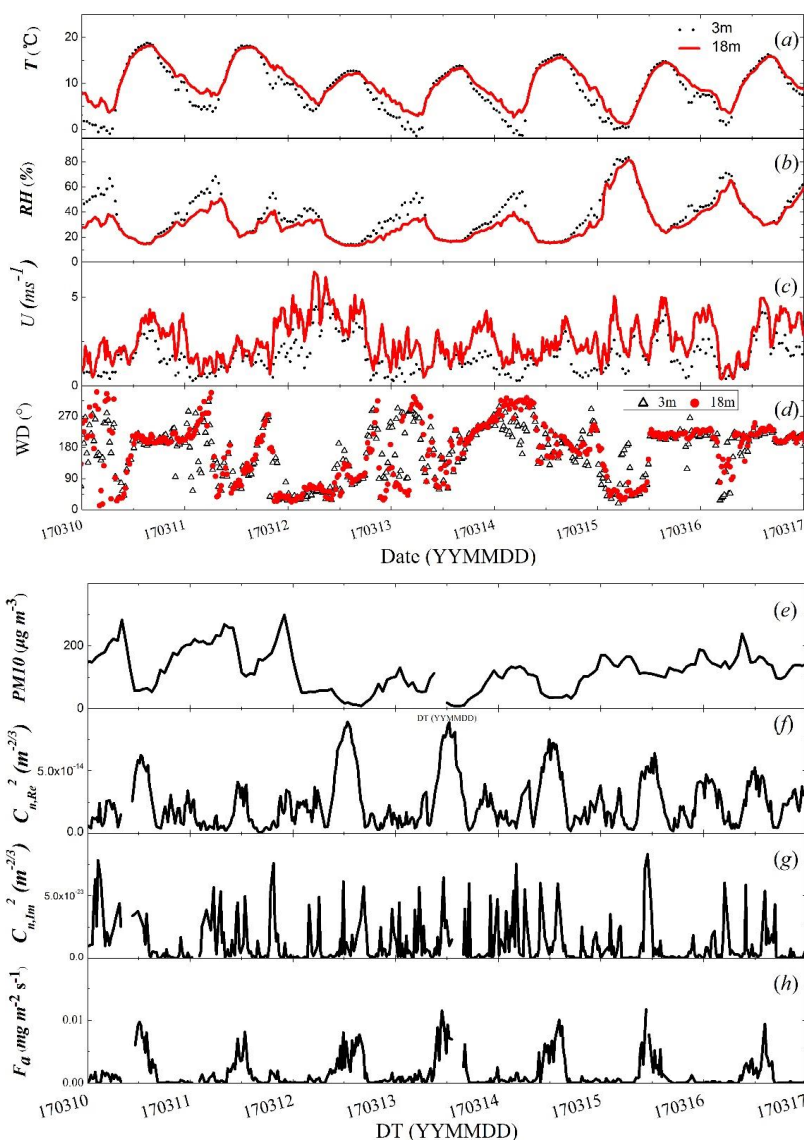
784 Figure 4. Temporal variations in (a) air temperature, (b) RH, (c) wind speed, (d) wind direction, (e) PM_{10},

785 (f) real part of the AERISP, (g) imaginary part of the AERISP and (h) aerosol mass flux in the Baoding

786 area from March 10, 2017 to March 17, 2017.

787
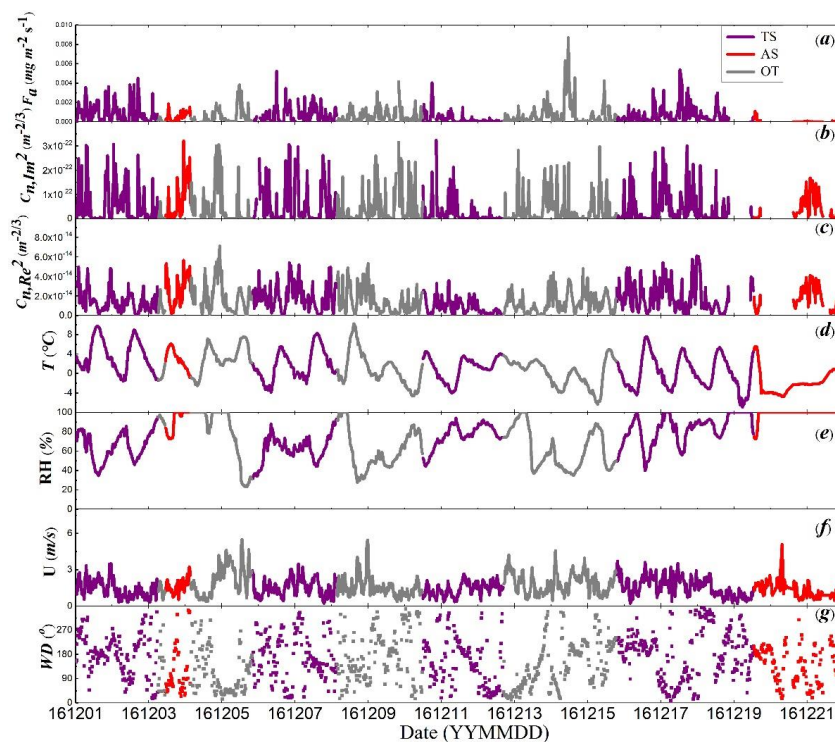
Figure 5. Temporal variations in (a) aerosol flux, (b) imaginary part of the AERISP, (c) real part of the AERISP (d) air temperature, (e) RH, (f) wind speed, and (g) wind direction in the Baoding area during a heavy pollution period, i.e., December 1, 2016 to December 22, 2016.

792
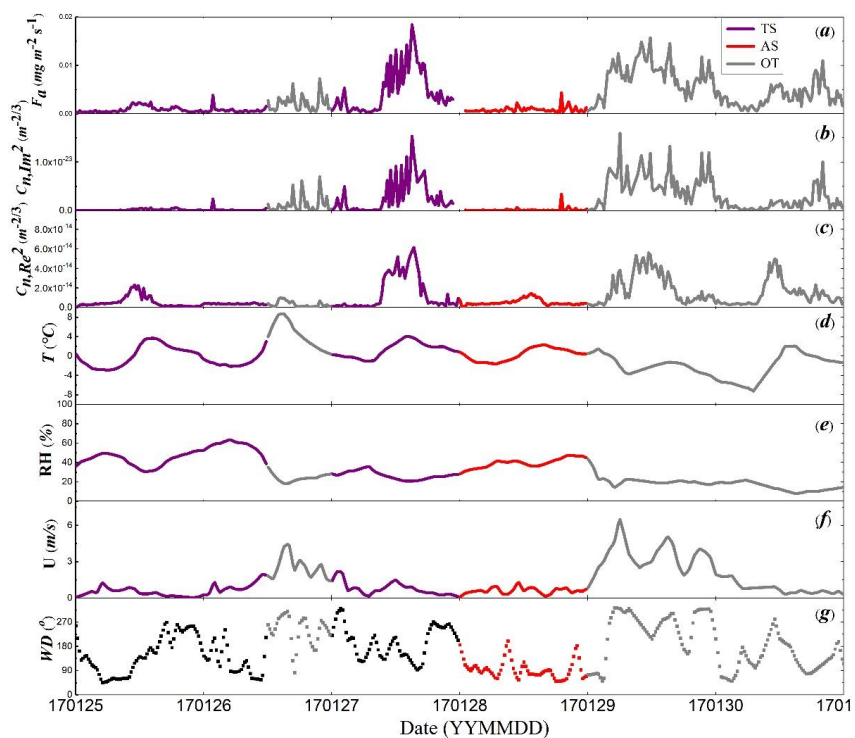
Figure 6. Temporal variations in (a) aerosol flux, (b) imaginary part of the AERISP, (c) real part of the
AERISP (d) air temperature, (e) RH, (f) wind speed, and (g) wind direction in the Beijing area
during a heavy pollution period, i.e., January 25, 2017 to January 31, 2017.

796